CHEMISTRY

High-speed imaging of ice nucleation in water proves the existence of active sites

Mark A. Holden[1,2,3]*†, Thomas F. Whale[1,2], Mark D. Tarn[1,3], Daniel O'Sullivan[1‡], Richard D. Walshaw[1], Benjamin J. Murray[1], Fiona C. Meldrum[2]*, Hugo K. Christenson[3]*

Understanding how surfaces direct nucleation is a complex problem that limits our ability to predict and control crystal formation. We here address this challenge using high-speed imaging to identify and quantify the sites at which ice nucleates in water droplets on the two natural cleavage faces of macroscopic feldspar substrates. Our data show that ice nucleation only occurs at a few locations, all of which are associated with micron-size surface pits. Similar behavior is observed on α-quartz substrates that lack cleavage planes. These results demonstrate that substrate heterogeneities are the salient factor in promoting nucleation and therefore prove the existence of active sites. We also provide strong evidence that the activity of these sites derives from a combination of surface chemistry and nanoscale topography. Our results have implications for the nucleation of many materials and suggest new strategies for promoting or inhibiting nucleation across a wide range of applications.

INTRODUCTION

The development of strategies to control crystallization processes promises the ability to generate particles with specific structures, sizes, and morphologies to promote or inhibit crystallization and to determine where crystals form. However, while there are many effective approaches for controlling crystal growth, control over nucleation— the point at which many of these properties are defined—has proven more challenging, and it remains very difficult to predictably promote nucleation using foreign particles or surfaces. This is at least in part due to the problems associated with studying nucleation processes. Although recent advances in electron microscopy (*1*, *2*) and synchrotron-based techniques (*3*, *4*) are providing new opportunities for studying nucleation processes (*5*, *6*), we still have a poor understanding of the factors that drive heterogeneous nucleation, particularly with respect to the complexities introduced by topographical and chemical imperfections that are invariably present on all substrates.

Here, we describe a study of ice nucleation in droplets of supercooled liquid water placed on macroscopic substrates of feldspar and α-quartz, both important components of atmospheric aerosols. Our goal was to identify and characterize the sites at which nucleation occurs. In addition to its importance in both natural and man-made environments, ice provides a beautiful model system. A single nucleation event causes the entire droplet to freeze rapidly such that high-speed video microscopy can be used to find the nucleation site's location on the substrate. This contrasts with traditional nucleation studies where it is impossible to identify the first-formed nuclei, and the final crystal population is inevitably a product of competitive growth. Our approach is also distinct from studies of ice nucleation from vapor, where it is not possible to quantify the activities of different sites.

By directly observing nucleation on these substrates, we demonstrate that nucleation only occurs at a very limited number of active sites and quantify the efficiency of these sites. This resolves a long-standing problem regarding ice nucleation and shows that substrate heterogeneities are the most important factor in determining the freezing temperature of water; we lastly prove the existence of "active sites" and the hierarchy of their effectiveness. Our data also demonstrate the importance of surface topography in promoting nucleation. While this study focuses on ice nucleation, there is growing evidence that the ability of topography to promote nucleation is quite general (*7*–*10*) and can potentially offer a new strategy for promoting nucleation.

RESULTS

We conducted experiments using macroscopic microcline feldspar LD3 samples that had been polished along the two natural cleavage planes (001) and (010). Feldspar is an important component of atmospheric aerosols and a very effective ice-nucleating agent (*11*). We pipetted a 1-μl drop of Milli-Q water onto the prepared substrate, which was integrated into a Perspex cell with a dry nitrogen flow to avoid water or ice films forming around the droplet (fig. S1). We then cooled the substrate at 1°C min^{-1} from 15°C to below the freezing point using a custom-made cold stage and used high-speed video microscopy to capture ice nucleation within individual droplets (Fig. 1A). Figure 1 (B and C) shows two typical sequences of video images taken at 3000 fps (frames per second) during the cooling of water droplets on the (010) and (001) oriented section of feldspar, respectively. The nucleation site can be identified as the point (white arrows) from which fast-growing dendrites of ice emerge after nucleation at $T = -13.7°$ and −12.6°C. Analysis of the images showed that the ice dendrites propagate from the nucleation site at ≈10 cm s^{-1}, which is consistent with the literature (*12*). Examination of the feldspar (010) and (001) sections with scanning electron microscopy (SEM) and atomic force microscopy (AFM) (Fig. 2 and figs. S2 and S3) showed that each nucleation site was contained within a micron-scale pore or crack. These features are characteristic of the specific microtextures (termed perthitic) present in alkali feldspars (*13*).

Individual droplets were also subjected to multiple freeze-thaw cycles to determine whether nucleation was stochastic—in which case it would occur at different spatial locations in every cycle due to the presence of many equally active sites in every droplet—or whether nucleation occurred at preferred active sites. For these particular feldspar samples, we analyzed nine droplets in this manner over 13 to 26 melting/freezing cycles on both (001) and (010) thin sections. The (010) and (001)

[1]School of Earth and Environment, University of Leeds, Leeds LS2 9JT, UK. [2]School of Chemistry, University of Leeds, Leeds LS2 9JT, UK. [3]School of Physics and Astronomy, University of Leeds, Leeds LS2 9JT, UK.
*Corresponding author. Email: m.a.holden@leeds.ac.uk (M.A.H.); f.meldrum@leeds.ac.uk (F.C.M.); h.k.christenson@leeds.ac.uk (H.K.C.)
†Present address: Chemistry, Physical Sciences and Computing, University of Central Lancashire, Preston PR1 2HE, UK.
‡Present address: NHS Digital, 1 Trevelyan Square, Boar Lane, Leeds LS1 6AE, UK.

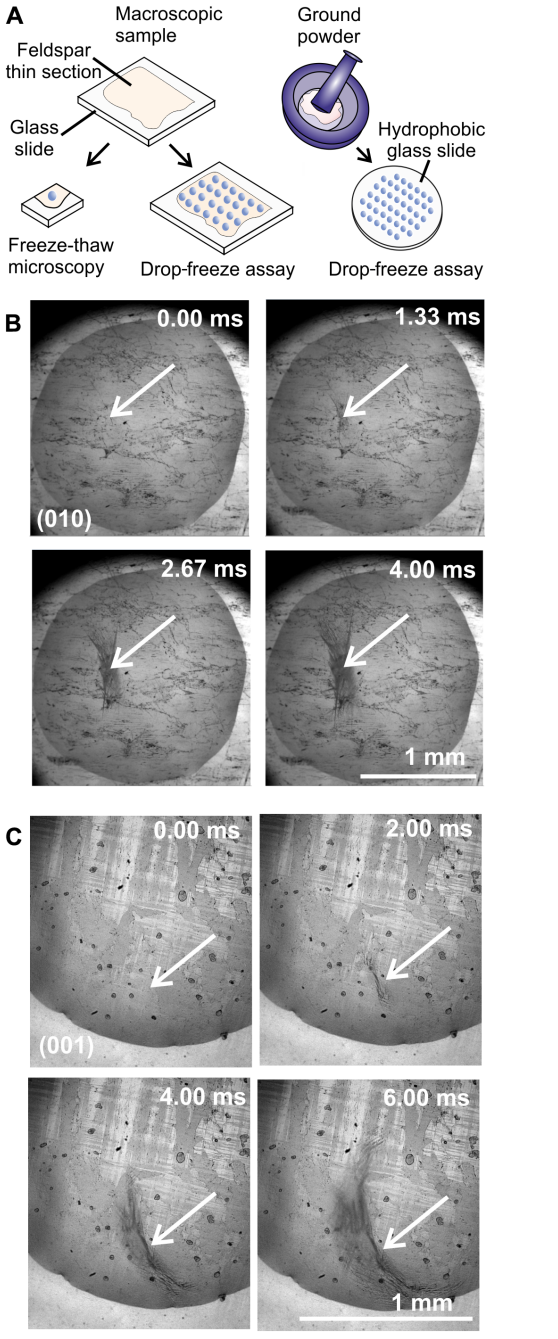

Fig. 1. Identification of ice nucleation sites on macroscopic feldspar. (**A**) Schematic showing the different experiments conducted in this study. (**B** and **C**) Sequence of images taken from individual freezing experiments of two separate droplets, on the (010) and (001) faces, respectively. A 1-µl droplet of water is placed on the feldspar thin section and cooled at 1°C min^{-1} until nucleation is detected with a high-speed camera operating at 3000 fps. The arrows show the region in which ice nucleated (see movies S1 and S2).

sections both exhibited comparable temperature ranges for nucleation [the average nucleation temperatures for four droplets on the (001) face and for five droplets on the (010) face were both −12.3°C]. Example data from four droplets, together with plots of the nucleation temperatures of the individual runs, are shown in Fig. 3, and data from a further four droplets are shown in fig. S4. Eight of nine droplets exhibited only three to five nucleation sites with a 2°C variation in nucleation temperature, but the one in fig. S4C showed eight sites with a 4°C variation in nucleation temperature. Notably, there is no pattern in the operation of these different active sites, and nucleation often switches back and forth between them. This demonstrates that the active sites are not substantially altered during these experiments.

The site-specific nature of nucleation on feldspar was also confirmed in freeze-thaw experiments, performed on arrays of drops on macroscopic feldspar (001) and (010) thin sections (Figs. 1A and 4A). The droplets were cooled at a constant ramp rate of 1°C min^{-1}, and their nucleation temperatures were identified optically and plotted as the fraction of droplets frozen as the temperature decreases (Fig. 4B). A strong correlation was again observed between the nucleation temperatures of each droplet on successive freeze-thaw cycles (example in Fig. 4D), which demonstrates that each droplet has a different typical nucleation temperature (*14*) and that the ice nucleation activity varies across the feldspar surface. For comparison, the average nucleation temperature of the nine macroscopic droplets has also been plotted in Fig. 4B (T_c freeze-thaw experiments), and it is within 0.5°C of the temperature at which the fraction frozen of the droplet arrays is 0.5.

These results were then compared with data from immersion-nucleation experiments on powders of the same feldspar, which were conducted by dispersing 0.1 to 1.0 wt % (weight %) of the powders in an array of 1 µl water droplets (Figs. 1A and 4B). Nucleation occurred at about 2°C lower temperatures for the droplets with 0.1 wt % feldspar powder but at ca. 2°C higher temperatures for the 1.0 wt % samples. To quantitatively compare these results, we need to normalize the droplet freezing probability (assumed equal to the fraction frozen) to the surface area of the nucleant available in each experiment.

The fraction-frozen plots in Fig. 4B, together with Brunauer-Emmett-Teller (BET) surface area measurements, allow the cumulative number of ice nucleation sites per unit surface area that become active upon cooling from 0°C to temperature T to be calculated (Fig. 4C and Materials and Methods) and compared with the same quantity for the droplets on the thin sections, where the area of contact between the droplet and the feldspar is used in the normalization. The solid line in this plot is taken from Atkinson *et al.* (*11*) and represents a "standard" microcline feldspar sample that is often used as a reference. Above $n_s(T) = 10\ cm^{-2}$, the thin section and immersed particle experiments have similar freezing temperatures, meaning that the macroscopic surfaces contain the same distribution of sites that control ice nucleation as the immersed particles. It is notable that, despite the differences in sample preparation, particle sizes, and other factors such as potential aggregation, the ice nucleation activities are very similar. Below $n_s(T) \approx 4\ cm^{-2}$, the immersed particles nucleate ice at higher temperatures than the macroscopic surfaces for the same active site density. The powdered samples hence have small densities of highly effective sites that are not found on the thin sections. Since the feldspar thin-section surface area under a droplet is close to the surface area of feldspar powder in the 0.1 wt % droplets (see Materials and Methods), the difference may be partly due to the creation or exposure of some very high activity sites during the grinding process, or the removal of sites from the thin sections by polishing, rather than due to sampling differences.

These experiments provide unique insight into the mechanism of heterogeneous ice nucleation, where there has been substantial discussion about whether the temperature variations seen experimentally during the freezing of water droplets containing nucleant particles are stochastic in origin or derive from active nucleation sites that exhibit varying nucleation temperatures. Data from many experiments have

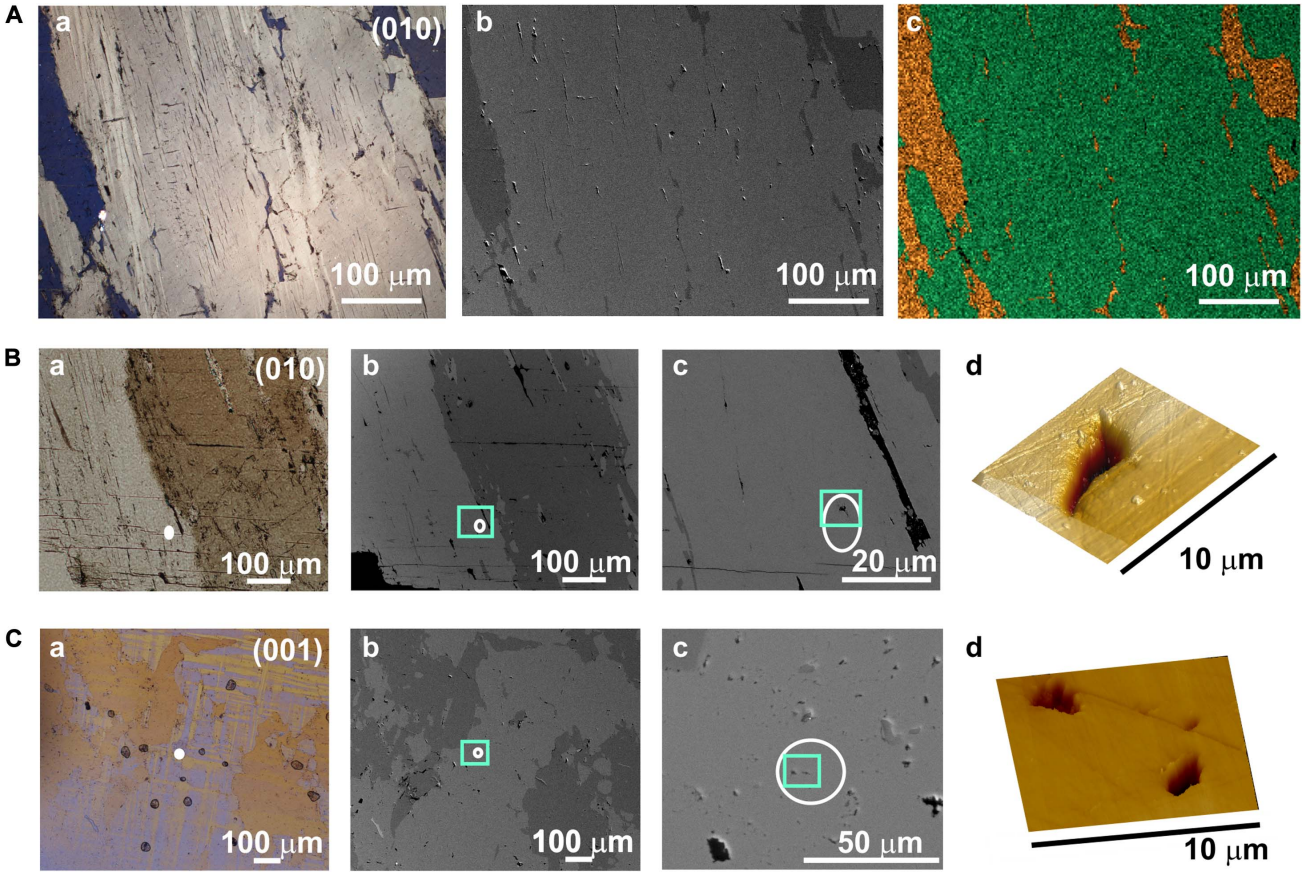

Fig. 2. Characterization of nucleation sites on feldspar thin sections. (**A**) Images demonstrating the exsolution microtexture. (**a**) Cross-polarized light micrograph showing Na^+-rich albite veins (blue) running through K^+-rich microcline. (**b**) Backscattered SEM micrograph showing the same region as in (a). The cracks in the surface (or micropores) that result from exsolution processes can be seen. The Na^+-rich region appears darker in these images. (**c**) Energy-dispersive x-ray (EDX) mapping of the region in (b) showing the separation of the cations into discrete regions. Two elements are presented as follows: Na^+ (gold) and K^+ (green). (**B** and **C**) Characterization of the regions corresponding to ice nucleation sites, where these are taken from (B) the (010) face and (C) the (001) face of feldspar, respectively. (**a**) Cross-polarized light micrographs of two regions, where veins of Na^+-rich albite regions (brown/orange) running through the K^+-rich (microcline) region are seen in (B) and the characteristic tartan twinning of the microcline region is observed in (C). (**b**) Backscattered SEM micrographs of the same region as in (a), where the darker regions correspond to Na^+-rich regions and the lighter regions correspond to K^+-rich regions. (**c**) Higher-magnification backscattered SEM micrographs, showing the features in the region highlighted by the green boxes in (b). (**d**) Three-dimensional projections of AFM micrographs obtained for a 100-μm^2 region containing the region in which ice formation began, as indicated in (c). In each case, deep pits, or micropores, are seen in the surface.

been successfully described by the "modified singular site model," which postulates that active sites exhibit characteristic nucleation temperatures, about which stochastic effects lead to slight temperature variations (*15*, *16*). Our study therefore provides direct evidence for the existence of active sites for nucleation from supercooled water, where a small number can potentially operate for a given nucleant particle.

Our experimental strategy also enables us to investigate the activities of the individual sites, where this is not possible by studying powders. Each nucleation site exhibits a distribution of nucleation temperatures (Fig. 5A), confirming that the probability of ice nucleation at individual sites varies with temperature (Fig. 5D and fig. S5). Whether more than one site operates within a droplet then depends on the overlap of the probability fields associated with each. When an overlap exists (Fig. 5D, e and f), the probability of nucleation at a temperature increases compared to the hypothetical case where only one of the sites is investigated, meaning that it is more likely that observations will be made at higher temperatures. The relative frequency of nucleation events at each site will depend on the relative probabilities of freezing at each site (Fig. 5D). The temperature range of freezing observed is then determined principally by the most active site(s) within the droplet. The data were also analyzed (as described in detail in the Supplementary Materials) to determine the nucleation rates of individual sites as a function of temperature (Fig. 5B and fig. S5, A and B). This is only possible when the vast majority of nucleation events occur at a single site (in this case, >88%). A comparison with the powdered feldspar samples was made by normalizing the data with respect to surface area (Fig. 5C). That the powders show a smaller slope than the individual sites is consistent with the fraction frozen curve being constructed from many droplets each with their own active site (section S1).

Last, we carried out experiments on ice nucleation on polished rose quartz (α-quartz) to explore whether a comparable mechanism operates on a different substrate. α-quartz nucleates ice relatively effectively (*17*, *18*) but undergoes conchoidal fracture and has less marked variations in substrate topography (fig. S6). We obtained a similar pattern of results for ice nucleation on a rose quartz surface, where a

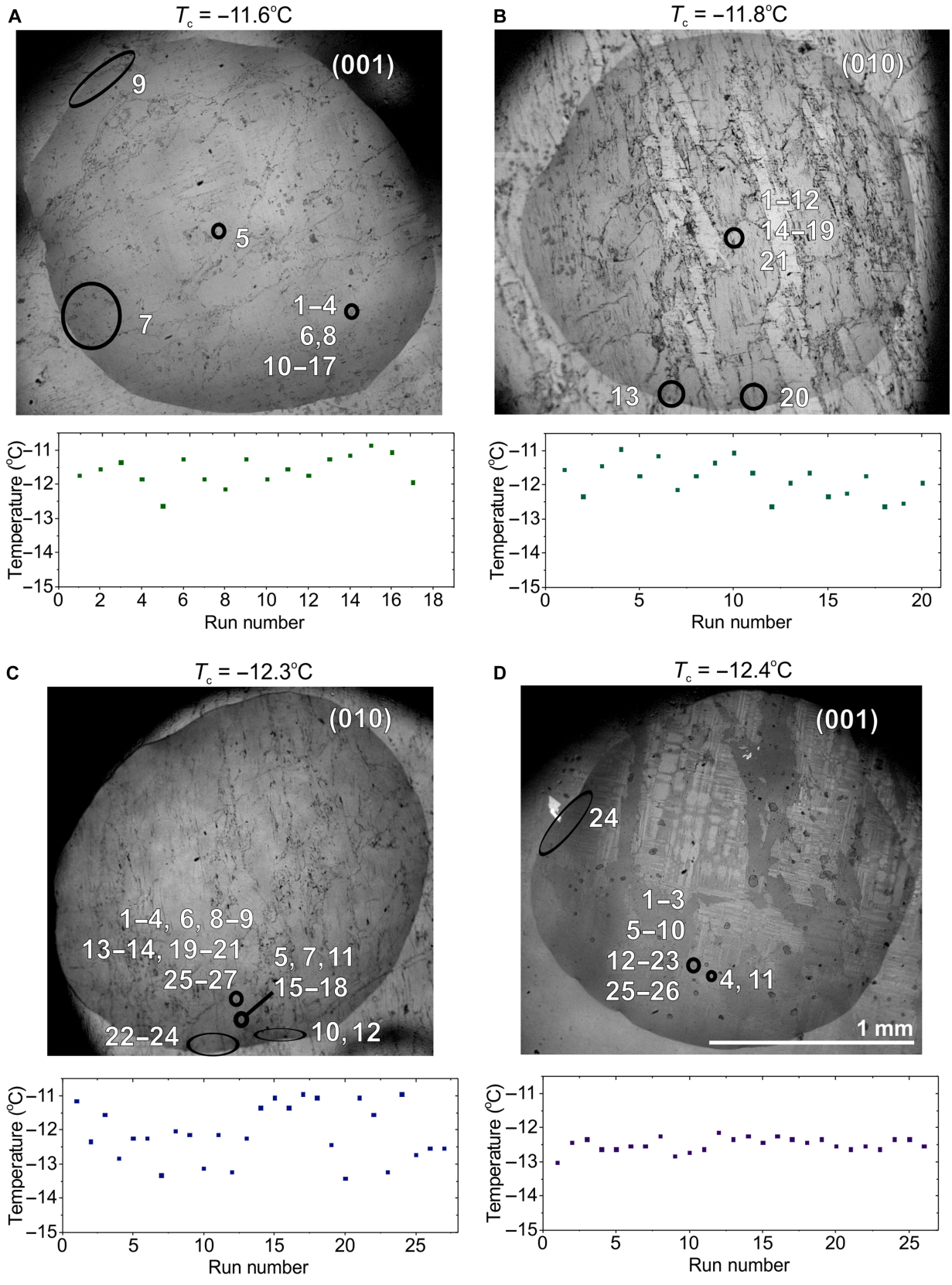

Fig. 3. Active site identification on feldspar from freeze-thaw experiments. (**A** to **D**) Light micrographs of water droplets on feldspar (001) and (010) sections showing the location of the nucleation sites for individual runs (numbered). Freezing began in the circled regions, and the characteristic nucleation temperature (T_c) for each droplet is shown. The nucleation temperatures for the individual experimental runs are shown below the light micrographs.

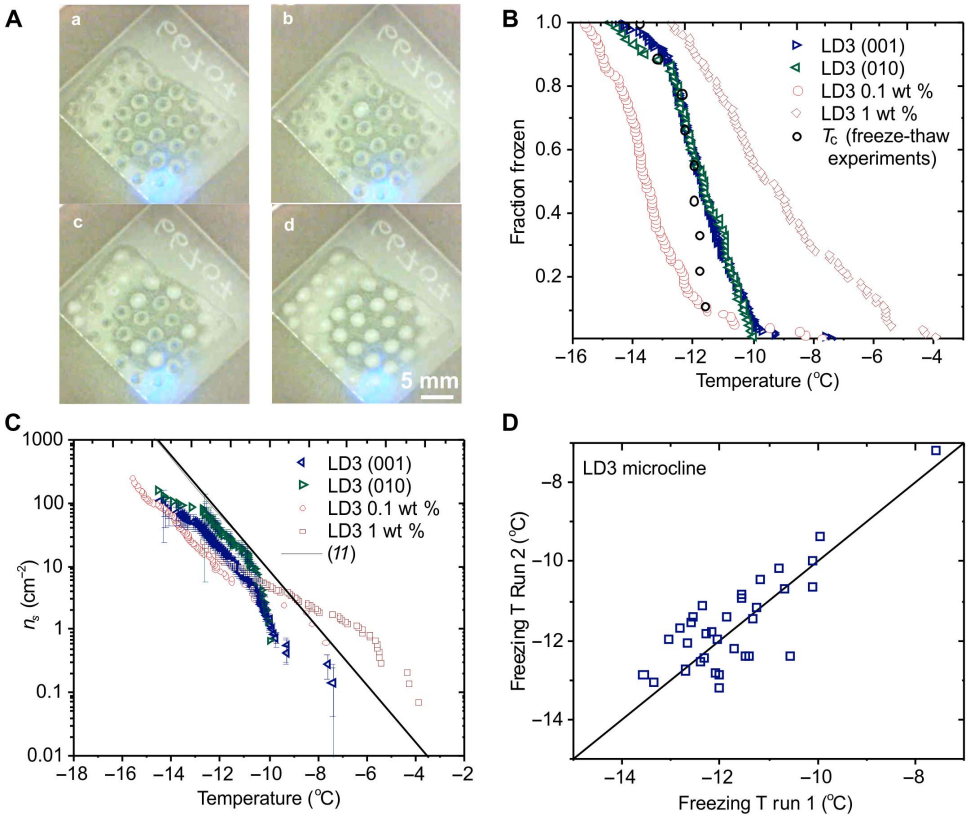

Fig. 4. Comparison of thin sections with ground, immersed particles. (**A**) (**a** to **d**) Images showing a freezing experiment for an array of water droplets on a feldspar thin section, where frozen droplets scatter more light. (**B**) Droplet fraction frozen as a function of temperature for LD3 microcline samples. Green and blue triangles represent thin sections prepared by cleaving along both the (010) and (001) faces, respectively. The clear red squares and circles represent the ground particles, immersed in the liquid droplets. (**C**) Active site density, $n_s(T)$, as a function of temperature for the data plotted in (B). In addition, plotted is a fit for BCS376 feldspar, made by Atkinson *et al.* (*11*) from data obtained in a similar microliter droplet experiment on a suspended powder of a typical alkali feldspar. (**D**) Correlation plot showing a comparison of nucleation temperatures between two freeze-thaw cycles for an array of water drops on an LD3 feldspar sample. The solid black line is the 1:1 line, along which the nucleation temperature would be the same for both cycles.

sequence of video images of ice nucleation at an individual site is shown in Fig. 6A, together with data from the freezing of two droplets over multiple freeze-thaw cycles (Fig. 6, B and C). These figures show that a few sites again dominated nucleation. However, the nucleation temperature was lower and had a slightly larger spread of $-23°C < T < -19°C$. The number of active sites perhaps (9 total) was also higher than for the feldspar samples for a similar number of runs (21 cycles).

DISCUSSION

The ability of certain substrates to promote ice nucleation attracts considerable attention. Epitaxial matching is often considered an important factor but does not guarantee activity; many crystals with good lattice matches to ice are ineffective nucleators (*19*, *20*), while other substrates can effectively nucleate ice, despite no obvious structural relationship (*21*). The organization of hydrogen bonds alongside properties such as surface charge and polarizability may therefore play crucial roles (*21*, *22*). There is also growing evidence that topographical features including surface pits (*19*), cracks (*23*), and steps (*24*, *25*) on the surfaces of effective nucleants are associated with their activity.

Most studies of heterogeneous ice nucleation from liquid water have used particulate nucleants (*26*) and thus cannot provide any information about the nature of the individual nucleation sites. Our strategy, in contrast, enables us to identify and characterize these sites. The SEM and AFM images (Fig. 2 and figs. S2 and S3) provide very strong evidence for the role of surface topography in promoting ice nucleation, where systematic studies using feldspar powders have shown no correlation between ice nucleation activities and the crystal structures or overall chemical compositions of the feldspars (*27*). These data also complement recent studies of ice nucleation from vapor, which have shown that ice crystals form at surface defects such as cracks and cavities (*8*, *28*–*30*).

Why then are these topographic features so effective in promoting ice nucleation? Our data, and those of others, suggest that a number of factors may contribute to this activity. In the first place, they may stabilize the ice critical nucleus, as predicted by classical nucleation theory and suggested for the nucleation of proteins (*9*) and organic solutes (*10*) from solution. This is also supported by simulations, which have shown that the optimal pore size is approximately the same size as the critical nucleus (*31*). The features identified by SEM and AFM (Fig. 2) are far too large to offer any direct effect on a critical nucleus, which is on the order of nanometers for ice. An estimate based on the AFM and SEM images suggests that fewer than one in a thousand of these features are involved in ice nucleation in each droplet. However, these active sites may contain nanoscale features such as nanotunnels [often associated

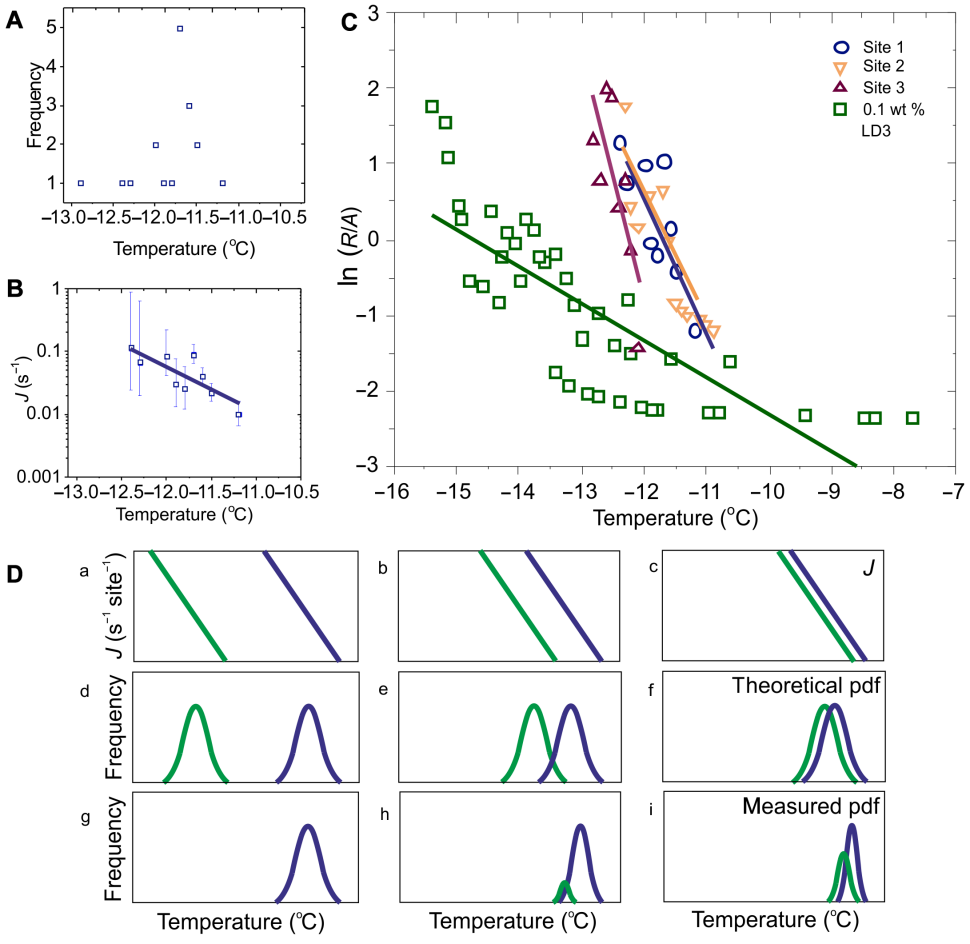

Fig. 5. Analysis of ice nucleation at active sites on feldspar. (**A**) Nucleation temperatures observed for the most active site in a droplet (shown in fig. S4D), where the frequency is the number of nucleation events at that temperature. (**B**) The site-specific nucleation rate, *J*, plotted against temperature, calculated, assuming that each cycle in the freeze-thaw experiments represents an individual droplet in an array. (**C**) Plot showing the nucleation rates (normalized by the surface area) of water on three sites on thin sections compared with that of a 0.1 wt % suspension of feldspar powder. (**D**) (**a** to **i**) Schematics showing three different examples of droplets containing two sites with differing nucleation rates *J*. In (a), *J* in the most active region (blue) is much higher than in the less active region (green). If each active site were isolated, the two theoretical probability density functions (pdfs) in (d) would be expected. With both sites in the same droplet, the probability density function in (g) is expected, with all nucleation at the most active site. In (b) and (c), the difference in *J* decreases, so there is more overlap in the theoretical probability density function in (e) and (f), leading to the expected experimental observations in (h) and (i). When nucleation is observed at two different sites, the measured characteristic nucleation temperature at each site is biased toward a higher temperature, giving a narrower measured distribution than in the equivalent "theoretical" case. Consequently, site-specific nucleation rates can only be calculated for active sites dominating the nucleation (e.g., >88% of observations here).

with perthitic microtextures (*27*)] that are of a size comparable to that of a critical nucleus.

The surface chemistry present within the defects sites is also vital. The surface of feldspar is largely hydroxylated, and the density and orientation of these groups are likely to be important in the nucleation effectiveness of an active site (*32*). Notably, Kiselev *et al.* (*29*) attributed the nucleation of ice from vapor at surface defects on alkali feldspars entirely to surface chemistry effects and suggested that unusual, high-energy (100) faces are present within effective nucleation sites that template the prismatic face of ice. In this context, it is interesting to highlight our results with rose quartz, which, similar to feldspar, exhibits a small number of very active sites. As rose quartz has no cleavage planes, this behavior cannot be attributed to the exposure of unusual crystal faces within defect sites, although it could be related to the exposure of surfaces with a high density of H-bonding sites.

In the specific case of nucleation from vapor, capillary condensation can occur within narrow pores (*33*, *34*), such that ice then nucleates from supercooled water rather than directly from vapor (*8*, *30*). The very concept of deposition-mode nucleation has recently been questioned, with claims that no clear evidence of ice formation directly from the vapor could be found in the literature (*35*). This mechanism could provide the basis for the preferential formation of ice crystals at defect sites on feldspar seen by Kiselev *et al.* (*29*), where we have shown that ice nucleation from vapor on muscovite mica occurs via condensates in wedge-like surface pores (*8*, *30*).

Modeling studies of ice nucleation within nanoscale graphene wedges have shown that nucleation rates were substantially enhanced at specific angles of the wedge (*36*). The different characteristic freezing temperatures of the sites would be due to subtle variations in surface chemistry such as density and configuration of functional groups. These arguments could explain why the most effective sites are also the scarcest;

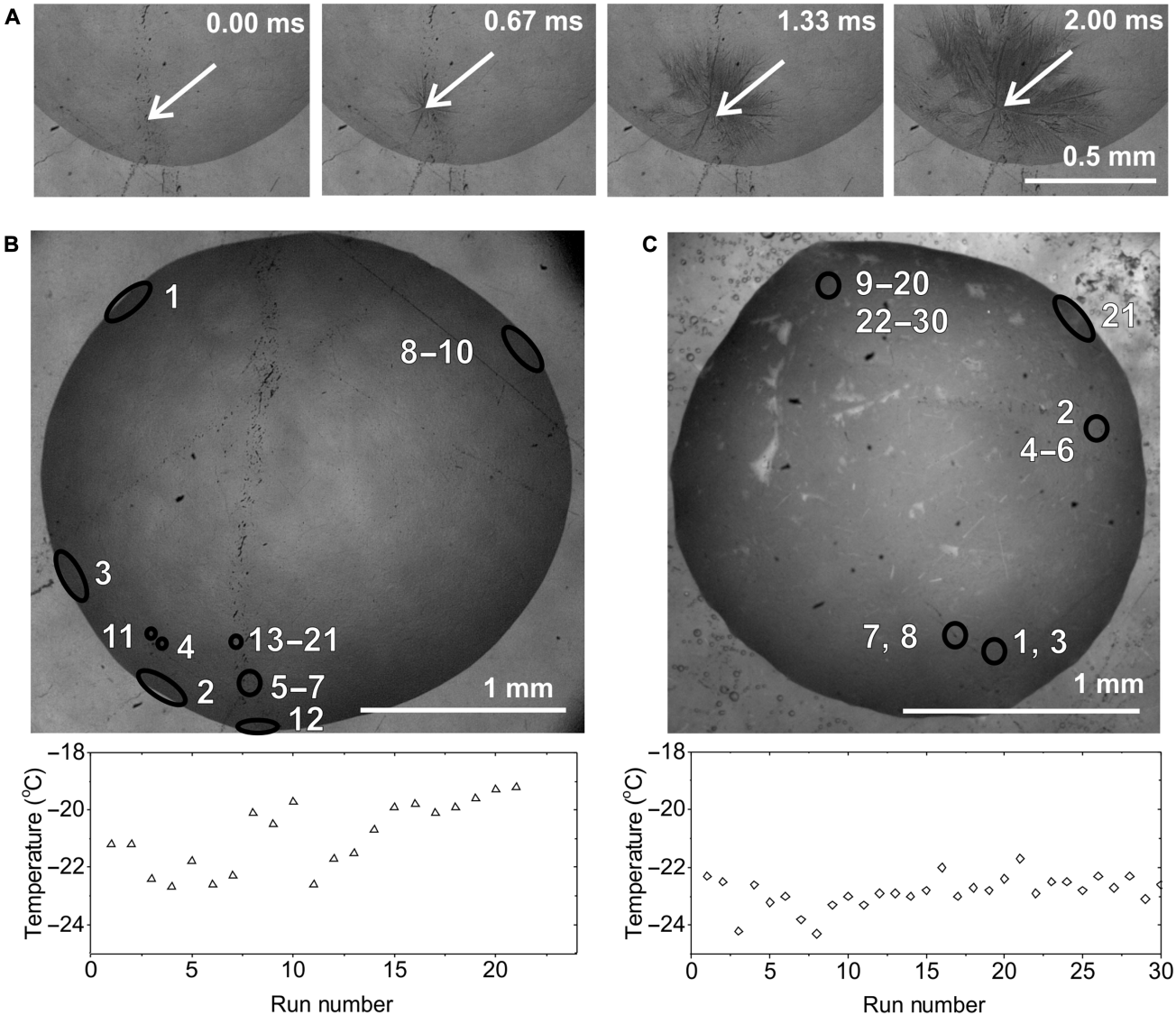

Fig. 6. Active site identification on rose quartz. (**A**) Sequence of light micrographs showing the site of ice nucleation in a water droplet on a rose quartz surface. Images were obtained at 3000 fps (see movie S3). (**B** and **C**) Light micrographs identifying the location of ice nucleation sites on the quartz surface during a freeze-thaw experiment. The numbers represent the cycle in which freezing occurred in the location marked by a circle. Plots of the temperatures at which nucleation occurred in each cycle of the freeze-thaw experiment are displayed below each micrograph.

these would comprise an optimal but unlikely synergy of topography and surface chemistry for nucleating ice.

CONCLUSIONS

In summary, we have combined high-speed imaging with freeze-thaw experiments on droplets to identify the sites at which ice nucleates from supercooled water on macroscopic substrates. Our study provides direct evidence for the existence of a small number of active sites and thus proves that substrate heterogeneities are the most important factor in determining the freezing temperature, with a secondary contribution from stochastic effects. The scarcity of these sites indicates that each exhibits a rare combination of defect geometry and surface chemistry and that an epitaxial match between the critical ice nucleus and substrate is not required. A growing body of evidence suggests that such topographical control over nucleation is by no means unique to ice. Our imaging-based methodology therefore offers a route by which substantial advances can be made in understanding heterogeneous nucleation and thus developing effective nucleants for applications as diverse as polymorph control of pharmaceuticals, scale prevention, and cryopreservation.

MATERIALS AND METHODS

Preparation of macroscopic substrates

The microcline feldspar LD3 was obtained from the University of Leeds mineral collection, where its phase had been previously confirmed by powder x-ray diffraction. (*37*). The rose quartz sample was from Baylis Quarry, Bedford, NY and was obtained from Excalibur Minerals Corporation (Charlottesville, VA, USA). Its phase (α-quartz) was confirmed

with Raman spectroscopy (fig. S7) (*38*). For experiments on macroscopic substrates, samples were prepared using standard petrographic thin-section preparation methods. Briefly, samples were initially wet-cut parallel to the desired cleavage plane to an initial thickness of around 2 mm. For LD3, these cuts were made parallel to the two cleavage planes, which were preidentified on the initial sample. For the rose quartz sample, which had no obvious faceting and no natural cleavage planes, the cut was made in an arbitrary direction. Their thickness was further reduced with a grinding wheel, before polishing with diamond pastes of sequentially smaller grain sizes down to 0.25 µm. Before experiments, substrates were cleaned using a dry ice cleaning system to remove large particles. The surface was then rinsed with isopropanol, followed by Milli-Q water, and then dried with a stream of nitrogen. Tests on thin sections showed that this process did not degrade or alter the ice nucleation activity of the substrate.

Ice formation on macroscopic substrates

Experiments were conducted using a homebuilt cold stage based on a temperature-controlled aluminum block with a hole in it for light transmission (fig. S1). A polycrystalline diamond slide, which has good thermal conductivity, was fixed on the aluminum block over this hole using thermal paste to create a cold surface of uniform temperature. Samples were placed onto the diamond window using a thin layer of vacuum grease. Cooling of the aluminum block was achieved using a liquid nitrogen flow, and the temperature was controlled by counter-heating with cartridge heaters embedded in the stage. The temperature was measured with a platinum resistance thermometer inserted into the aluminum block. The cold stage was mounted onto an Olympus BX53 light microscope, and a Phantom Miro 320 high-speed camera was used to collect freezing videos at 3000 fps. A Perspex cell with an inlet and an outlet for gas was placed around the sample. The bottom of this cell sat on the aluminum block, or on the edge of the thin section depending on the sample size, while the top contained a hole into which the microscope objective was lowered. A flow of zero-grade nitrogen was applied to the inlet to remove water from the atmosphere within the cell to avoid condensation of water onto the substrate as it was cooled.

Experiments were conducted by pipetting a 1-µl drop of Milli-Q water (18.2 megohm·cm) onto the selected substrate. The Perspex cell was then placed around the sample, the stage was raised to focus on the sample surface, and the drop was then cooled at a constant 1°C min^{-1} from 15°C until the droplet froze. The high-speed camera was operated using the Phantom Camera Control software. During operation, the camera would constantly record to its internal memory at the desired framerate and resolution. When ice nucleation was observed, the software was triggered. This stopped the recording, and the data that had been recorded to memory over the previous 1.5 s, containing the nucleation event, were stored. At the point of triggering, the temperature measurement displayed on the Eurotherm 2416 was recorded. Once a freezing event was recorded, the Eurotherm 2416 controller was used to raise the temperature to 5°C at a heating rate of 5°C min^{-1} to allow the drop to melt. The temperature was held until no ice remained in the drop, typically for 1 min, and then the cooling cycle was restarted at 1°C min^{-1}. Each experiment comprised between 10 and 30 of these freeze-thaw cycles. For drops that froze at lower temperatures, a higher nitrogen flow rate was typically required to avoid freezing by communication via water condensed on the substrate. In total, nine separate experiments were performed using LD3 microcline, each on different regions of the feldspar surface. Five different thin sections were used in these experiments [three with (010) orientation and two with (001) orientation]. For rose quartz, two experiments in different locations on the surface of one thin section were performed.

The temperature uncertainty within an individual freeze-thaw experiment was estimated as 0.2°C, determined by measuring the melting points of water, dodecane and undecane, as used by Whale *et al.* (*39*). This uncertainty is consistent with that estimated by Atkinson *et al.* (*11*) using the same cold stage. Between experiments, that is, when a new area was investigated and freeze-thaw cycles restarted, the temperature uncertainty increased to ca. 1°C, due to factors such as the varying thermal conductivity of different thin sections. In all cases, these experiments were performed on glass slides of the same thickness as those used for preparing thin sections to minimize uncertainties from thermal gradients.

Ice formation with powdered nucleants

Nucleation experiments were conducted with arrays of 1-µl Milli-Q water droplets with 0.1 and 1 wt % suspended feldspar particles, obtained by grinding LD3 microcline using an agate pestle and mortar. These were carried out using the "microliter Nucleation by Immersed Particles Instrument" (µl-NIPI), as described previously by Whale *et al.* (*39*). Thirty to 50 drops were pipetted onto a 22-mm-diameter hydrophobic silanized slide placed on a cryocooler inside a Perspex cell with a gas inlet and outlet. Zero-grade nitrogen was flowed through at 300 sccm (standard cubic centimeters per minute), and the sample was cooled at a rate of 1°C min^{-1} from 15° to −40°C. Freezing events were identified from an optical recording by a webcam, and the corresponding freezing temperature was obtained from the temperatures recorded by the cryocooler software. A minimum of two runs of each suspension were performed. This technique was repeated for macroscopic feldspar samples, where the silanized slide was replaced by a thin section. A minimum of two thin sections of each orientation were measured in this manner. The freeze-thaw data presented in the correlation plot in Fig. 4D were collected in the same manner as for single-drop cryomicroscopy experiments but using the µl-NIPI technique to investigate an array of drops simultaneously.

Analysis of ice formation experiments

The temperature/frequency plot, equivalent to a probability density function, for an individual site was plotted using the recorded temperatures, in 0.1°C bins, for freezing events at a specific site. By considering sequential freeze-thaw cycles as one experiment on an array of several drops containing the exact same site, a fraction frozen (f.f.) could be calculated as

$$\text{f.f.} = n(T)/N$$

where $n(T)$ is the number of droplets frozen at temperature T and N is the total number of droplets. This is plotted in fig. S5 (A and B). This consideration can also be used to calculate the site-specific nucleation rate, J, using

$$\frac{\Delta n}{N_1} = (1 - \exp(-J\Delta t))$$

where Δn is the number of drops that freeze in time increment Δt and N_1 is the total number of unfrozen drops at the start of the time increment Δt. Note that this differs from N above, which relates to the total number of drops in an experiment. To compare the site-specific nucleation rates to the bulk freezing rate, R/A, data from these freeze-thaw cycles at specific sites are compared to data from arrays of drops

containing ground powders [note that, for arrays, freezing rate is used rather than nucleation rate following the terminology of Vali (*16*) since the freezing rate and nucleation rates are not equivalent for multiple component systems]. This can be calculated from

$$\frac{\Delta n}{N_1} = (1 - \exp(-R\Delta t A))$$

where R is the freezing rate and A is the surface area per drop. The surface area of nucleant per drop was measured in two ways. For immersed ground particles, the surface area was calculated using the BET-specific surface area of the ground sample and the mass of particles in suspension. The specific surface area measured was 1,78 $m^2\ g^{-1}$ for LD3 microcline. For the thin sections, the area of the drops was used to calculate the surface area of feldspar in contact with water; this was measured using ImageJ software, with the width of the thin-section glass slide measured with digital Vernier calipers as a reference measurement.

To investigate whether the thin sections contain ice nucleation sites of the same activity as those in the powders, we compared the ice nucleation effectiveness of arrays of water drops on the macroscopic feldspar to arrays of drops containing the ground, immersed powders using the surface active site density, n_s (T) (Fig. 4C). This is the cumulative number of ice nucleation sites per unit surface area that become active upon cooling from 0°C to temperature T and is calculated as

$$\frac{n(T)}{N} = 1 - \exp(-n_s(T)A)$$

where $n(T)$ is the number of droplets frozen at temperature T, N is the total number of droplets in the experiment, and A is the surface area per droplet. In using this approximation, it is assumed that the time dependence of nucleation arising from the stochastic nature of ice nucleation is negligible and that the freezing temperature is principally determined by the presence of different site(s) in different drops. The surface area per drop is calculated as above. The surface area of feldspar covered by a 1-μl water drop on a thin section was 0.025 ± 0.004 cm^2. The surface area of feldspar in a 1-μl drop was 0.0194 cm^2 for 0.1 wt % and 0.194 cm^2 for 1 wt % suspensions.

Uncertainties were calculated by propagating the surface area measurement uncertainties with the Poisson uncertainties, as described in Harrison *et al.* (*37*). The contact angles (measured using an FTA4000 video system) of water droplets on the feldspar thin sections were typically 50°. Contact angles were not measured for rose quartz, but the similar surface area covered by water drops of similar volume suggests a similar contact angle.

Analysis of substrates and powders

The macroscopic substrates were characterized using a Nikon Eclipse LV100 polarizing microscope in transmitted light mode to confirm their orientations and characterize their microtexture (*13*). Further information about the surface structures of the substrates was obtained using SEM, where this was conducted using an FEI Nova NanoSEM 450 microscope operating with an Everhart-Thornley detector or a circular backscatter detector. Images were recorded in both backscattered electron and secondary electron modes. Samples were mounted on aluminum stubs using double-sided Cu tape and sputter-coated with a 2-nm Ir layer for imaging or carbon-coated for energy-dispersive x-ray (EDX) analysis. EDX measurements were obtained using the same microscope, and EDX maps were recorded at 18 kV, selecting for K^+, Na^+, and Ca^{2+}, cations which are commonly found in feldspars.

AFM was used to determine the size and shape of the features observed in the region where ice nucleated. Micrographs were recorded in contact mode using a Bruker MultiMode 8 AFM with a NanoScope V controller. Images were collected at 0.5 to 2 Hz using silicon nitride cantilevers with a nominal spring constant of 0.35 Nm^{-1} (model SNL-10, Bruker).

Wavelength-dispersive spectroscopy (WDS) was used to perform precise elemental analyses on a targeted area. Before the measurement, four active sites were identified using the cryomicroscopy method. These were then targeted to measure the concentrations of specific elements typically found in trace quantities in feldspar in and around the region of nucleation, to see whether a higher concentration of these elements was present at the active sites. Measurements were obtained using a JEOL 8230 electron probe microanalyzer operating with 8 kV of accelerating voltage. Samples were carbon-coated before measurements, and Ba-L_α, Fe-L_α, Pb-M_α, Rb-L_α, and Sr-L_α emissions were recorded. Fe-K_α was not used as this would have required a higher accelerating voltage, which is associated with more rapid sample degradation over the scan time, and a higher electron beam penetration depth. From AFM measurements, the topography at the active sites had depths of <200 nm, so a lower penetration depth would give an analysis that was likely more targeted at the active site. No increased signal was observed at the active sites (see fig. S8); one hot spot was observed for Fe, as identified in fig. S8A (b), but this was not in the region that ice nucleated. Therefore, within the resolution of the technique used, the local chemistry at the active sites was no different from that of the surrounding feldspar surface.

SUPPLEMENTARY MATERIALS

Supplementary material for this article is available at http://advances.sciencemag.org/cgi/content/full/5/2/eaav4316/DC1

Supplementary Text
Section S1. Time dependence of nucleation
Section S2. Nucleation at the contact line
Section S3. Morphology of growing ice
Fig. S1. Schematic of experimental setup.
Fig. S2. Identification of feldspar active sites.
Fig. S3. Microscopy of feldspar active sites.
Fig. S4. Identification of active sites through freeze-thaw experiments.
Fig. S5. Time dependence of nucleation.
Fig. S6. Identification of rose quartz active sites.
Fig. S7. Characterization of rose quartz.
Fig. S8. WDS maps of active sites.
Fig. S9. Investigation of freezing at the three-phase line.
Movie S1. Ice nucleation from the melt on the (010) face of microcline feldspar.
Movie S2. Ice nucleation from the melt on the (001) face of microcline feldspar.
Movie S3. Ice nucleation from the melt on α-quartz.
Movie S4. Movie demonstrating how freeze-thaw video microscopy can be used for direct observation of site-specific ice nucleation in supercooled water.
References (*40*, *41*)

REFERENCES AND NOTES

1. P. J. M. Smeets, A. R. Finney, W. J. E. M. Habraken, F. Nudelman, H. Friedrich, J. Laven, J. J. De Yoreo, P. M. Rodger, N. A. J. M. Sommerdijk, A classical view on nonclassical nucleation. *Proc. Natl. Acad. Sci. U.S.A.* **114**, E7882–E7890 (2017).
2. A. E. S. Van Driessche, N. Van Gerven, P. H. H. Bomans, R. R. M. Joosten, H. Friedrich, D. Gil-Carton, N. A. J. M. Sommerdijk, M. Sleutel, Molecular nucleation mechanisms and control strategies for crystal polymorph selection. *Nature* **556**, 89–94 (2018).
3. E. D. Bøjesen, B. B. Iversen, The chemistry of nucleation. *CrystEngComm* **18**, 8332–8353 (2016).

4. M. Zobel, A. Windmüller, E. M. Schmidt, K. Götz, T. Milek, D. Zahn, S. A. J. Kimber, J. M. Hudspeth, R. B. Neder, The evolution of crystalline ordering for ligand-ornamented zinc oxide nanoparticles. *CrystEngComm* **18**, 2163–2172 (2016).
5. P. J. M. Smeets, K. R. Cho, R. G. E. Kempen, N. A. J. M. Sommerdijk, J. J. De Yoreo, Calcium carbonate nucleation driven by ion binding in a biomimetic matrix revealed by in situ electron microscopy. *Nat. Mater.* **14**, 394–399 (2015).
6. E. M. Pouget, P. H. H. Bomans, J. A. C. M. Goos, P. M. Frederik, G. de With, N. A. J. M. Sommerdijk, The initials stages of template-controlled $CaCO_3$ formation revealed by cryo-TEM. *Science* **323**, 1455–1458 (2009).
7. J. L. Holbrough, J. M. Campbell, F. C. Meldrum, H. K. Christenson, Topographical control of crystal nucleation. *Cryst. Growth Des.* **12**, 750–755 (2012).
8. J. M. Campbell, F. C. Meldrum, H. K. Christenson, Observing the formation of ice and organic crystals in active sites. *Proc. Natl. Acad. Sci. U.S.A.* **114**, 810–815 (2017).
9. N. E. Chayen, E. Saridakis, R. P. Sear, Experiment and theory for heterogeneous nucleation of protein crystals in a porous medium. *Proc. Natl. Acad. Sci. U.S.A.* **103**, 597–601 (2006).
10. Y. Diao, A. S. Myerson, T. A. Hatton, B. L. Trout, Surface design for controlled crystallization: The role of surface chemistry and nanoscale pores in heterogeneous nucleation. *Langmuir* **27**, 5324–5334 (2011).
11. J. D. Atkinson, B. J. Murray, M. T. Woodhouse, T. F. Whale, K. J. Baustian, K. S. Carslaw, S. Dobbie, D. O'Sullivan, T. L. Malkin, The importance of feldspar for ice nucleation by mineral dust in mixed-phase clouds. *Nature* **498**, 355–358 (2013).
12. M. Schremb, J. M. Campbell, H. K. Christenson, C. Tropea, Ice layer spreading along a solid substrate during solidification of supercooled water: Experiments and modeling. *Langmuir* **33**, 4870–4877 (2017).
13. I. Parsons, J. D. Fitz Gerald, M. R. Lee, Routine characterization and interpretation of complex alkali feldspar intergrowths. *Am. Mineral.* **100**, 1277–1303 (2015).
14. A. Peckhaus, A. Kiselev, T. Hiron, M. Ebert, T. Leisner, A comparative study of K-rich and Na/Ca-rich feldspar ice-nucleating particles in a nanoliter droplet freezing assay. *Atmos. Chem. Phys.* **16**, 11477–11496 (2016).
15. R. J. Herbert, B. J. Murray, T. F. Whale, S. J. Dobbie, J. D. Atkinson, Representing time-dependent freezing behaviour in immersion mode ice nucleation. *Atmos. Chem. Phys.* **14**, 8501–8520 (2014).
16. G. Vali, Interpretation of freezing nucleation experiments: Singular and stochastic; sites and surfaces. *Atmos. Chem. Phys.* **14**, 5271–5294 (2014).
17. T. Zolles, J. Burkart, T. Häusler, B. Pummer, R. Hitzenberger, H. Grothe, Identification of ice nucleation active sites on feldspar dust particles. *J. Phys. Chem. A* **119**, 2692–2700 (2015).
18. T. F. Whale, M. A. Holden, T. W. Wilson, D. O'Sullivan, B. J. Murray, The enhancement and suppression of immersion mode heterogeneous ice-nucleation by solutes. *Chem. Sci.* **9**, 4142–4151 (2018).
19. P. Conrad, G. E. Ewing, R. L. Karlinsey, V. Sadtchenko, Ice nucleation on BaF_2(111). *J. Chem. Phys.* **122**, 064709 (2005).
20. V. Sadtchenko, G. E. Ewing, D. R. Nutt, A. J. Stone, Instability of Ice Films. *Langmuir* **18**, 4632–4636 (2002).
21. N. Fukuta, B. J. Mason, Epitaxial growth of ice on organic crystals. *J. Phys. Chem. Solids* **24**, 715–718 (1963).
22. S. J. Cox, S. M. Kathmann, B. Slater, A. Michaelides, Molecular simulations of heterogeneous ice nucleation. I. Controlling ice nucleation through surface hydrophilicity. *J. Chem. Phys.* **142**, 184704 (2015).
23. C. Marcolli, B. Nagare, A. Welti, U. Lohmann, Ice nucleation efficiency of AgI: Review and new insights. *Atmos. Chem. Phys.* **16**, 8915–8937 (2016).
24. G. W. Bryant, J. Hallett, B. J. Mason, The epitaxial growth of ice on single-crystalline substrates. *J. Phys. Chem. Solids* **12**, 189–195 (1960).
25. B. J. Anderson, J. Hallett, Supersaturation and time dependence of ice nucleation from the vapor on single crystal substrates. *J. Atmos. Sci.* **33**, 822–832 (1976).
26. Z. A. Kanji, L. A. Ladino, H. Wex, Y. Boose, M. Burkert-Kohn, D. J. Cziczo, M. Krämer, Overview of ice nucleating particles. *Meteorol. Monogr.* **58**, 1.1–1.33 (2017).
27. T. F. Whale, M. A. Holden, A. N. Kulak, Y.-Y. Kim, F. C. Meldrum, H. K. Christenson, B. J. Murray, The role of phase separation and related topography in the exceptional ice-nucleating ability of alkali feldspars. *Phys. Chem. Chem. Phys.* **19**, 31186–31193 (2017).
28. B. Wang, D. A. Knopf, S. China, B. W. Arey, T. H. Harder, M. K. Gilles, A. Laskin, Direct observation of ice-nucleation events on individual atmospheric particles. *Phys. Chem. Chem. Phys.* **18**, 29721–29731 (2016).
29. A. Kiselev, F. Bachmann, P. Pedevilla, S. J. Cox, A. Michaelides, D. Gerthsen, T. Leisner, Active sites in heterogeneous ice nucleation—The example of K-rich feldspars. *Science* **355**, 367–371 (2017).
30. J. M. Campbell, H. K. Christenson, Nucleation- and emergence-limited growth of ice from pores. *Phys. Rev. Lett.* **120**, 165701 (2018).
31. A. J. Page, R. P. Sear, Heterogeneous nucleation in and out of pores. *Phys. Rev. Lett.* **97**, 065701 (2006).
32. P. Pedevilla, M. Fitzner, A. Michaelides, What makes a good descriptor for heterogeneous ice nucleation on OH-patterned surfaces. *Phys. Rev. B* **96**, 115441 (2017).
33. H. K. Christenson, Two-step crystal nucleation via capillary condensation. *CrystEngComm* **15**, 2030–2039 (2013).
34. T. Kovács, F. C. Meldrum, H. K. Christenson, Crystal nucleation without supersaturation. *J. Phys. Chem. Lett* **3**, 1602–1606 (2012).
35. C. Marcolli, Deposition nucleation viewed as homogeneous or immersion freezing in pores and cavities. *Atmos. Chem. Phys.* **14**, 2071–2104 (2014).
36. Y. Bi, B. Cao, T. Li, Enhanced heterogeneous ice nucleation by special surface geometry. *Nat. Commun.* **8**, 15372 (2017).
37. A. D. Harrison, T. F. Whale, M. A. Carpenter, M. A. Holden, L. Neve, D. O'Sullivan, J. Vergara Temprado, B. J. Murray, Not all feldspars are equal: A survey of ice nucleating properties across the feldspar group of minerals. *Atmos. Chem. Phys.* **16**, 10927–10940 (2016).
38. K. J. Kingma, R. J. Hemley, Raman spectroscopic study of microcrystalline silica. *Am. Mineral.* **79**, 269–273 (1994).
39. T. F. Whale, B. J. Murray, D. O'Sullivan, T. W. Wilson, N. S. Umo, K. J. Baustian, J. D. Atkinson, D. A. Workneh, G. J. Morris, A technique for quantifying heterogeneous ice nucleation in microlitre supercooled water droplets. *Atmos. Meas. Tech.* **8**, 2437–2447 (2015).
40. C. Gurganus, A. B. Kostinski, R. A. Shaw, High-speed imaging of freezing drops: Still no preference for the contact line. *J. Phys. Chem. C* **117**, 6195–6200 (2013).
41. C. W. Gurganus, J. C. Charnawskas, A. B. Kostinski, R. A. Shaw, Nucleation at the contact line observed on nanotextured surfaces. *Phys. Rev. Lett.* **113**, 235701 (2014).

Acknowledgments: We thank J. H. Wyn Williams for the preparation of petrographic thin sections and A. Kulak for help with SEM and EDX measurements. **Funding:** This project was supported by the Engineering and Physical Sciences Research Council grants EP/M003027/1 (to H.K.C., F.C.M., and B.J.M.) and EP/N002423/1 (to F.C.M. and H.K.C.), the Leverhulme Trust RPG-2014-306 (to H.K.C.), and the European Research Council 713664 CryoProtect and 648661 Marinelce (T.F.W. and B.J.M.). **Author contributions:** B.J.M., F.C.M., and H.K.C. conceived and ran the project. M.A.H. designed and conducted all experiments and analysis. T.F.W., M.D.T., and D.O. assisted in the experimental design. M.D.T. assisted with temperature calibrations and D.O. assisted with uncertainty analysis. M.A.H., T.F.W., and R.D.W. ran electron microprobe experiments. M.A.H., B.J.M., T.F.W., H.K.C., and F.C.M. wrote the paper. **Competing interests:** The authors declare that they have no competing interests. **Data and materials availability:** All data that support the findings of this study are available in the Research Data Leeds Repository with the identifier [http://doi.org/10.5518/411]. All data needed to evaluate the conclusions in the paper are present in the paper and/or the Supplementary Materials. Additional data related to this paper may be requested from the authors.

Submitted 14 September 2018
Accepted 17 December 2018
Published 1 February 2019
10.1126/sciadv.aav4316

Citation: M. A. Holden, T. F. Whale, M. D. Tarn, D. O'Sullivan, R. D. Walshaw, B. J. Murray, F. C. Meldrum, H. K. Christenson, High-speed imaging of ice nucleation in water proves the existence of active sites. *Sci. Adv.* **5**, eaav4316 (2019).

Science Advances

High-speed imaging of ice nucleation in water proves the existence of active sites

Mark A. Holden, Thomas F. Whale, Mark D. Tarn, Daniel O'Sullivan, Richard D. Walshaw, Benjamin J. Murray, Fiona C. Meldrum and Hugo K. Christenson

Sci Adv **5** (2), eaav4316.
DOI: 10.1126/sciadv.aav4316